

NEW GRID INDENTATION METHOD FOR MULTIPHASE MATERIALS

JIRÍ NOHAVÁ^{a*} and PETR HAUŠILD^b

^a CSM Instruments, Rue de la Gare 4, CH-2034 Pesieux, Switzerland, ^b Czech Technical University in Prague, Faculty of Nuclear Sciences and Physical Engineering, Department of Materials, Trojanova 13, 120 00 Praha 2, Czech Republic
jno@csm-instruments.com

Keywords: Nanoindentation; Stainless steel; Martensitic transformation

1. Introduction

Instrumented indentation or shortly nanoindentation is very powerful technique for characterization of materials in small volumes. Despite its undoubted contribution to the measurements of mechanical properties care must be taken during experiments to correctly understand the obtained results while testing certain types of materials.

Among such materials belong non-homogeneous (multiphase) materials whose indentation testing is complicated especially when the dimensions of the phases are unmatched. Even very high positioning precision is not always sufficient in such cases to differentiate between the phases.

The measurement parameters of indentation on non-homogeneous materials shall not affect the results which is important especially in cases where the cracking or the stress/strain induced phase transformations can occur. On the one hand, the indent should be sufficiently small in order to distinguish the tiny phases. On the other hand, the interaction of the indenter tip with surface becomes complex contact problem especially for low indentation depths when rounding of the indenter tip can play an important role. Moreover, growing popularity of using low loads brings up another problem known as indentation size effect, which affects mainly the hardness values^{1–3}. Consequently the hardness can be used only for comparative purposes in this load range.

Compared to standard indentation using Vickers indenter and measurement of the imprint's diagonals, instrumented indentation is based on recording of the force and indentation depth data. The so obtained curve is then used for calculation of hardness. The hardness calculation is not based on optical observation and can therefore be done automatically. Additionally, important material characteristics such elastic modulus and energy of indentation can be calculated from the indentation data record. Finally, as the calculation of hardness and elastic modulus is calcu-

lated by the indentation software, automated series of measurements can be done. This is particularly useful when large statistical datasets are required which is the case in the grid indentation method⁵. This method is based on several hundreds of indentations and their subsequent statistical evaluation. The grid indentation method is used for calculation of local mechanical properties of multiphase materials in which satisfactory results cannot be obtained by other techniques or single indentations. The application of this method on material with different volume fraction of two phases and its results are subject of this paper.

The low-nickel metastable austenitic stainless steel was chosen as it undergoes the deformation-induced phase transformation of face-centered cubic (fcc) γ austenite to body-centered cubic (bcc) α' -martensite and hexagonal closed packed (hcp) ε -martensite⁶. The ε -martensite forms from randomly spaced overlapping stacking faults while the α' -martensite forms at shear band intersections^{7–9}. During straining, the volume fraction of α' -martensite rapidly prevails over the volume fraction of ε -martensite and the α' -martensite grows at the expense of the ε -martensite. High internal stresses are generated due to an incompatible transformation strain accompanying the martensitic transformation. The good knowledge of local properties of austenitic and martensitic phases is therefore an essential constituent for modeling the material behavior of metastable austenitic steels subjected to plastic strain.

2. Experimental details

The material chosen for this paper was experimental steel provided by the ARCELOR-MITTAL. The chemical composition is given in Tab. I and corresponds to the AISI 301 grade. The low nickel and chromium content situates the steel at the limit of the austenite field in the Schaeffler's diagram¹⁰. The material was supplied as cold rolled sheets of 0.68 mm thickness in the bright annealed state.

The measurements were performed on samples in the initial state and on the tensile pre-deformed specimens. Strain level was chosen $\varepsilon = 0.1$ (10 %) and $\varepsilon = 0.2$ (20 %) of logarithmic (true) deformation in order to obtain the microstructure with predominant austenitic phase

Table I
Chemical composition of AISI 301 steel (in wt. %)

	C	Cr	Ni	Si	Mn	Mo
Nominal	max 0.12	16–18	6.5–9	<1.5	<2	<0.8
Analyzed	0.05	17	7	0.5	1.5	0.1

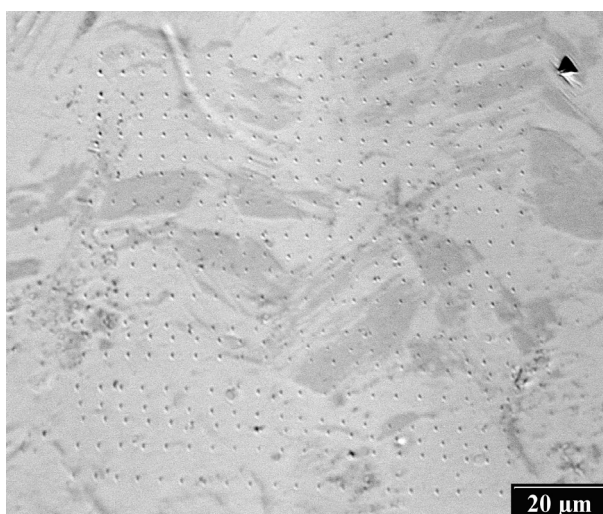


Fig. 1. Indentation grid on 10 % pre-deformed sample: light gray – austenite, dark gray – martensite

($\varepsilon = 10\%$) and α' -martensitic phase ($\varepsilon = 20\%$), in both cases with low fraction of ε -martensite.

Surface of samples was electro-polished in 5 % perchloric acid solution in ethanol at 40 V to avoid the surface layer affected by mechanical grinding and polishing, which can itself produce the deformation induced martensitic transformation.

Nanindentation measurements were performed on CSM Instruments NHT Nano Indentation Tester with Berkovich indenter using instrumented indentation technique. The NHT uses passive top referencing concept which almost entirely eliminates the thermal drift and is therefore ideal for several hours taking grid indentation method. The indentation parameters chosen from preliminary experiments were as follows: maximum load 1 mN, loading rate 6 mN min^{-1} , unloading rate 6 mN min^{-1} , 5 s hold at the maximum load. The grid indentation was performed on predeformed samples with different martensite volume fraction. Several randomly selected rectangular areas in dimensions of $100 \mu\text{m} \times 100 \mu\text{m}$ were tested on each sample. The indentation matrix on each of such areas comprised 20×20 indentations equidistantly spaced by $5 \mu\text{m}$ (Fig. 1).

Electron back scattered diffraction (EBSD) analysis was carried out in scanning electron microscope FEI Quanta 200 FEG equipped with a TSL™ EBSD analyzer. The samples were inspected at a tilt angle of 70° . Acquired data were evaluated by OIM™ software.

3. Results and discussion

Figure 2 shows typical force versus indentation depth record as obtained on stainless steel and fused silica. The areas corresponding to elastic and plastic work of indenta-

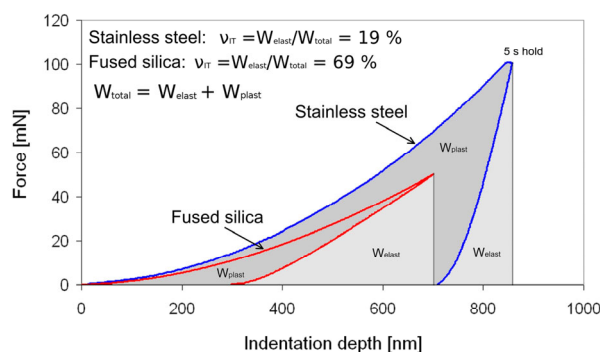


Fig. 2. Typical force versus indentation depth curve

tion are gray shaded. For the samples tested in this study, the maximum indentation depth varied from about 77 nm (in the deformed material) to 90 nm (in the non-deformed material) for maximum load of 1 mN.

The results of grid indentation in form of dataset were treated statistically in order to extract the properties of single phases by fitting the data using appropriate distribution function. The hardness values were selected for the statistical evaluation as the Young's moduli of austenite and martensite are very close. The elastic to total work of indentation ratio v_{IT} was also less correlated with the phase occurrence than hardness and it was therefore not considered for statistical treatment.

The hardness values measured on austenite in non-deformed state matched the Gaussian distribution (see Fig. 3). Bimodal Gaussian distribution function (I) was in the first instance chosen to describe the grid indentation results obtained on pre-deformed (two-phase) samples:

$$f = \frac{1-p}{\sqrt{2\pi}\sigma_1} \exp\left[-\frac{(H_{IT} - \mu_1)^2}{2\sigma_1^2}\right] + \frac{p}{\sqrt{2\pi}\sigma_2} \exp\left[-\frac{(H_{IT} - \mu_2)^2}{2\sigma_2^2}\right] \quad (1)$$

where H_{IT} is the hardness, p is the mixing parameter, and μ_1 , σ_1 , μ_2 , σ_2 are the parameters of distribution.

The parameters of distribution were identified by maximum likelihood method using Generalized Reduced Gradient nonlinear optimization¹¹. The identification is slightly complicated by the fact that the peaks of distribution are overlapping.

It can be seen that with increasing pre-deformation the hardness increases and the distribution changes from right-hand tailed to left-hand tailed as the martensite volume increases (Fig. 3). Further, the deformation of remaining austenite is constrained by the martensite laths and its apparent hardness therefore increases.

In the second step, the area containing the indentation grid was analyzed by EBSD. The martensite volume fraction f_m obtained by EBSD is in fairly good agreement with the mixing parameter p of the fitted bimodal Gaussian

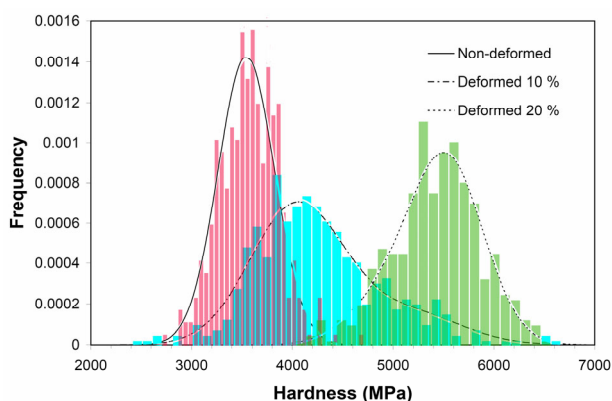


Fig. 3. Comparison of hardness distribution on all three tested samples

distribution function. For both pre-deformation, the predominant phase is slightly overestimated by the fitting parameter of bimodal Gaussian distribution (79 % comparing to 76 % in the case of 10 % predeformation and 81 % comparing to 79 % in the case of 20 % predeformation).

Subsequently the perimeter of $0.5 \mu\text{m}$ was traced around each indent and the measured hardness values were sorted in cases belonging to austenitic (A), austenitic and martensitic (A+B) and martensitic (B) according to occurrence (see Fig. 4 for schematic representation). It should be noted that even if we do not know how far the phases extend under the surface, the indentation depth is fairly low compared to the chosen surrounding area size so one can expect that in the majority of cases this classifying is correct.

The distributions identified separately on austenite and/or martensite indentation cases were compared with the apparent bimodal distribution as obtained by Gaussian fit. The apparent distribution leads to slight over- and un-

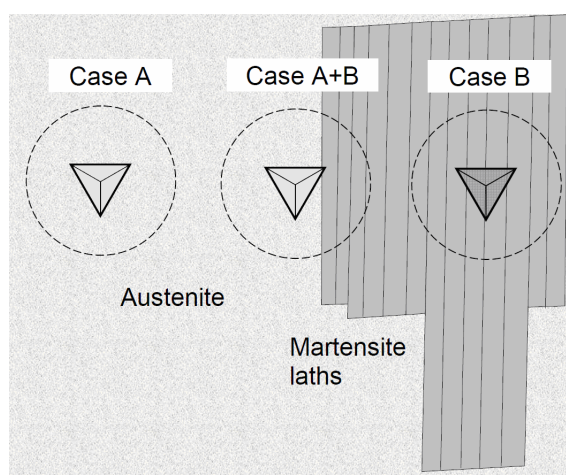


Fig. 4. Three principle cases of indentation: austenitic (A), austenitic and martensitic (A+B) and martensitic (B)

der-estimation of the μ_1 and μ_2 mean hardness values of austenitic and martensitic phases respectively. The scatters of both austenitic and martensitic phases σ_1 , σ_2 are slightly higher for the apparent distribution than for the distributions identified separately.

Nevertheless, the discrepancy between the parameters obtained for the apparent distribution and for the distributions identified separately is relatively low (less than 5 %) so that the parameters obtained by the apparent distribution can be taken as the first approximation of the real behavior.

4. Conclusions

The application of the grid indentation method on austenitic steel with pressure induced transformations is shown in this paper. The results of the experiments confirm that this method can be used for estimation of mechanical properties of materials with two phases even if these are unmatched. The phase volume fractions and the distribution of hardness in each phase at different strain levels were determined by the instrumented indentation and statistical analysis with reasonable accuracy. The EBSD results confirmed the volume fraction of each phase as found by the statistical analysis of the indentation experiments. The grid indentation method can be used on multiphase materials for calculations of single phase properties which are hardly accessible by other measurement techniques. The so obtained results are indispensable for correct modelling of mechanical behaviour of these materials.

This work was carried out in the frame of research project MSM 6840770021. Arcelor-Mittal group is acknowledged for preparing the experimental material.

REFERENCES

- Gane N.: Proc. Royal Society A 317(1530), 367 (1970).
- Kreuzer H.G.M., Pippan R.: Mater. Sci. Eng., A 387–389, 254 (2004).
- Kreuzer H.G.M., Pippan R.: Mater. Sci. Eng., A 400–401, 460 (2005).
- Randall N.X., Vandamme M., Ulm F.-J.: J. Mater. Res. 24, 679 (2009).
- Mangonon Jr. L., Thomas G.: Metall. Trans. 1, 1577 (1970).
- Suzuki T., Kojima H., Suzuki K., Hashimoto T., Ichihara M.: Acta Met. 25, 1151 (1977).
- Brooks J.W., Loretto M.H., Smallman R.E.: Acta Met. 27, 1839 (1979).
- Humbert M., Petit B., Bolle B., Gey N.: Mater. Sci. Eng., A 454–455, 508 (2007).
- Schaeffler A.L.: Metal Progr. 56, 680 (1949).
- Fylstra D., Lasdon L., Warren A., Watson J.: Interfaces 28, 29 (1998).

J. Nohava^a and P. Haušild^b (^a *CSM Instruments, Czech Technical University in Prague, Faculty of Nuclear Sciences and Physical Engineering, Department of Materials*): **New Grid Indentation Method for Multiphase Materials**

Mechanical properties of metastable austenitic steel were investigated using a novel grid indentation method. Under deformation martensitic laths are formed in this steel. As the martensite laths are of submicrometric dimen-

sions, single spot nanoindentation failed and the grid indentation method had to be used. The method was applied on samples with three levels of predeformation. A matrix of 800 indentations was done on each sample. The results were plotted in form of a histogram and statistically evaluated using bimodal Gaussian distribution. The results allowed estimation of the hardness of the martensite laths and the austenite matrix. The volume fraction of martensite was also calculated and it corresponded well to the results obtained by the EBSD.

MECHANICAL PROPERTIES AND STRUCTURE OF Zr-Nb ALLOY AFTER HIGH-TEMPERATURE TRANSFORMATIONS

JAN ŘÍHA*, OLGA BLÁHOVÁ,
and PAVOL ŠUTTA

New Technologies – Research Centre, University of West Bohemia, Univerzitní 8, 306 14, Plzeň, Czech Republic
janriha@ntc.zcu.cz

Keywords: Zirconium alloys, In situ X-ray diffraction analysis, Phase transformations, Indentation hardness

1. Introduction

Zirconium alloys are indispensable part of materials used in nuclear reactors already 50 years. With regard to their excellent corrosion resistance in water at high temperatures and having very low effective cross-section capture of thermal neutrons, zirconium alloys are used as protective layers of nuclear fuel rods¹.

Presently the development is focused on behaviour of Zr-alloys during Loss - Of - Coolant - Accident. In this case integrity and dimension stability of the components are the key parameters. During the rapid heating up to 1000 °C the accelerated oxidation takes place and subsequent fast quenching leads to deterioration of their mechanical properties. Mainly the hardness is growing up whereas the ductility is falling down^{1,2}.

At high temperatures proceeds also the phase transformation of zirconium from α -phase (hexagonal close - packed lattice) to β -phase (body centered cubic lattice). Current temperature of transformation strongly depends on impurity elements presence in zirconium. Niobium causes

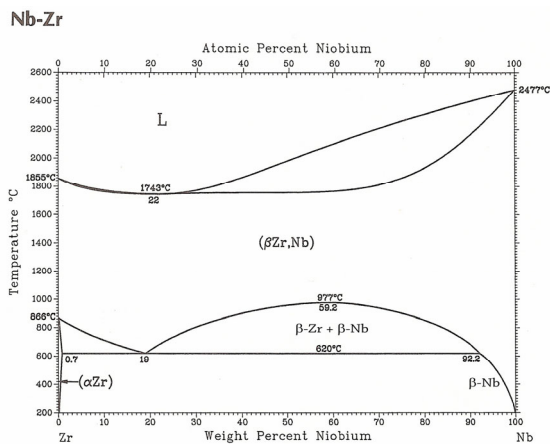


Fig. 1. Binary phase diagram of Zr – Nb system (ref.⁴)

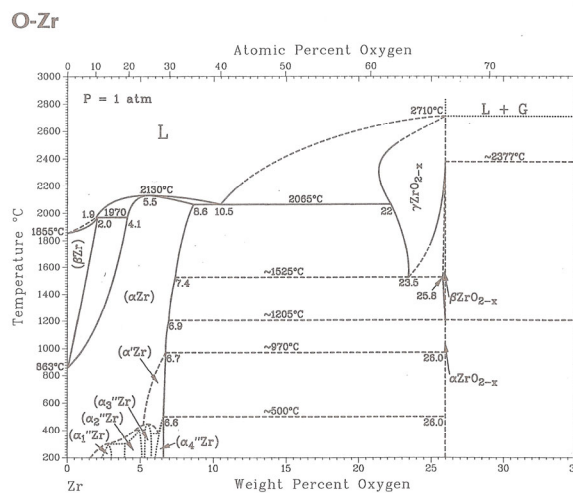


Fig. 2. Binary phase diagram of Zr – O system (ref.⁴)

a movement of transformation to lower temperatures whereas the oxygen to higher temperatures² (Fig. 1, 2).

This paper is focused on an interpretation of phase transformations and mechanical properties changes after high temperature processing.

2. Experiment

For the experiment the E110G Zr alloy was used. Initial semiproducts were in form of weldless tubes with outer diameter 9 mm and 0.7 mm wall thickness. These tubes were cut up into 11 mm wide rings. The rings were halved and mechanically compressed into a plane. Their surface was grinded and polished and then etched by an acid mixture of HNO₃, HCl and HF. The influence of plastic deformation caused by mechanical flattening was removed during the high-temperature exposition. The chemical composition of alloys is presented in Tab. I.

The *in situ* X-ray diffraction phase analysis was carried out on a Panalytical X'Pert Pro automatic powder diffractometer. This machine is equipped with a copper X-ray tube with K α radiation ($\lambda_{K\alpha} = 0.154$ nm) and high-temperature chamber Anton Paar HTK 1200 N. This device enables an equable heating up to 1200 °C and can be

Table I
Chemical composition of experimental material

Nb [wt.%]	H [ppm]	N [ppm]	C [ppm]	O [ppm]
1,0 ÷ 1,1	3	20	100	840

filled by an inert gas or evacuated. In this case a rotary oil pump with liquid nitrogen trap was used. For comparison one sample was measured also under vacuum created by a turbomolecular pump.

For the illustration of crystalline state an automatic powder diffractometer AXS Bruker D8 Discover was used analysing the lateral profile of the (002) line. This diffractometer is equipped with a cobalt X-ray tube ($\lambda_{K\alpha} = 0.179$ nm) and an area detector HI – STAR.

With a view to previous measurements published in³, the samples were exposed to the temperature 1000 °C. The deaeration of the sample surface during the heating was a very serious problem. That is why the temperature had to be increased very slowly for complete deaeration, which markedly influenced the size of crystallites.

For investigated samples, different deaeration temperatures were used. The first one was without deaeration, the temperature for the second one was 100 °C and 250 °C for the third one. Summary of the investigated samples and conditions is in Tab. II. The heating courses of some samples are in Fig. 3 and 4.

Measuring range for *in situ* measurements was from 25° to 75° 2 θ scale. The diffraction patterns were collected in initial state at room temperature, during the deaeration, at the exposition temperature and after the cooling at the

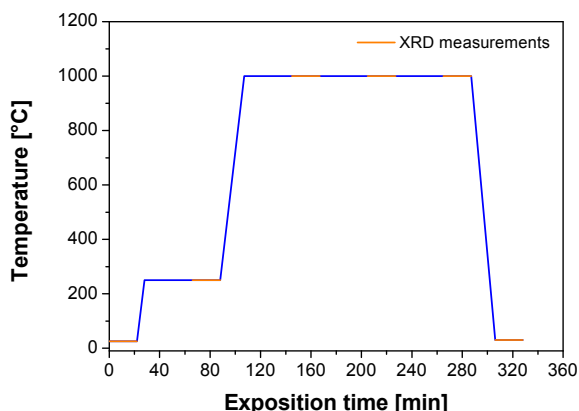


Fig. 3. Heating course for rotary pump

Table II
Experimental samples and conditions

Sample	Vacuum pump	Exposition temperature [°C]	Deaeration temperature [°C]
0201	Rotary	1000	0
0202	Rotary	1000	100
0203	Rotary	1000	250
0207	Turbo-molecular	1000	250

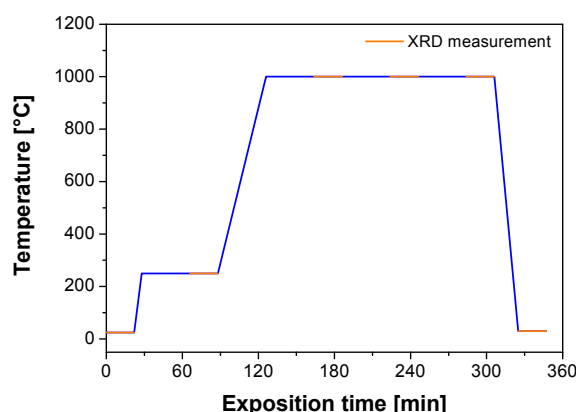


Fig. 4. Heating course for turbomolecular pump

temperature 30 °C. During the high-temperature exposition the samples were measured three times for better examination of the phase transformations. The pressure created by a rotary pump during the measurements was about $6 \cdot 10^{-1}$ Pa.

Measurements performed on AXS Bruker D8 diffractometer were collected in the range $25^\circ \pm 103^\circ$ 2 θ .

The indentation hardness measurements were carried out on a NanoIndenter XP with Berkovich indenter as a value in depth of 2 μ m. Sixty-five indents were created on the sample surface and the resulting values of indentation hardness and modulus of elasticity were obtained as mean values.

3. Results and discussion

Results of diffraction phase analysis show that the structure of all samples was in initial state created by α -phase of zirconium and with a trace amount of zirconium hydride ZrH. The ZrH phase was possible to identify according to a single diffraction line (111) with 100 %

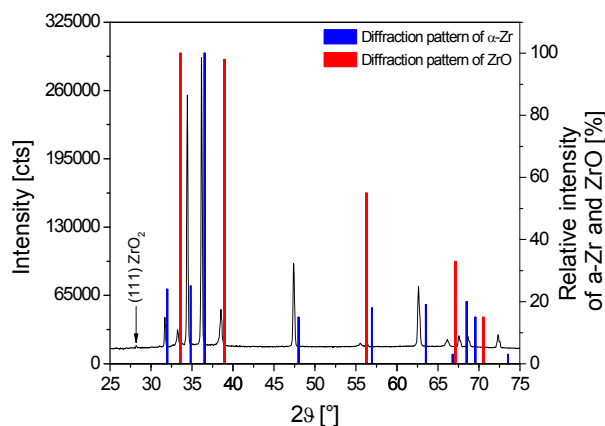


Fig. 5. The first diffraction pattern of sample 0203 at 1000 °C with referential diffraction patterns of α -Zr and ZrO

relative intensity. At high temperatures the ZrH phase disintegrated and the free gaseous hydrogen escaped from the samples. The first diffraction patterns of sample 0201 showed an influence of deaeration step absence, Fig. 6. There is a corrosion layer markedly seen on the surface.

This layer was composed of monoclinic oxide ZrO_2 and non-stoichiometric tetragonal oxide $\text{ZrO}_{1.99}$. A cubic oxide ZrO was also identified in the structure. A decreasing amount of surface oxides is seen in the second diffraction patterns of the same sample as a consequence of its transformation. A surface oxide layer represented only by a trace amount of ZrO_2 is seen in the third diffraction pattern.

The same phase composition was identified in diffraction patterns of samples 0202 and 0203 during the whole high-temperature exposition and also after the cooling, Fig. 7, 8. The measurements carried out at 1000 °C also showed that the transformation of α -Zr to β -Zr did not proceed. In all diffraction patterns only lines of α -phase of zirconium were identified.

This is probably caused by higher free oxygen amount in interstitial places of Zr matrix, which markedly increased the $\alpha \rightarrow \beta$ transformation temperature. The diffraction lines shift observed in all diffraction patterns is caused by thermal dilativity and partially also by crystallographic lattice expansion due to interstitial oxygen, Fig. 5.

Diffraction patterns of sample 0207 measured under vacuum $2 \cdot 10^{-3}$ Pa indicate that even here the phase transformation did not take place. Except of α -phase zirconium the ZrO and a trace amount of ZrO_2 were identified. In diffraction patterns of all samples measured at 1000 °C it is evident a growth in amount of ZrO phase, Fig. 6–8. This indicates that ZrO is not a part of surface corrosion layer but that it is in inner alloy volume.

The results from AXS Bruker D8 show an expressive influence of heating course on size of the crystallites, Fig. 9. All samples in initial state were rather finegrained – their lines are smooth and continuous.

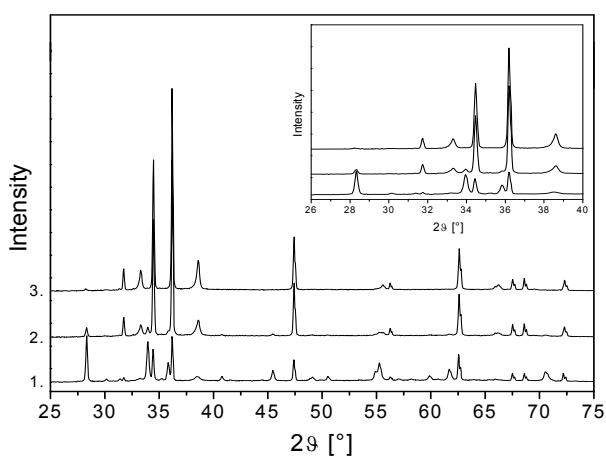


Fig. 6. Diffraction patterns of sample 0201 at 1000 °C

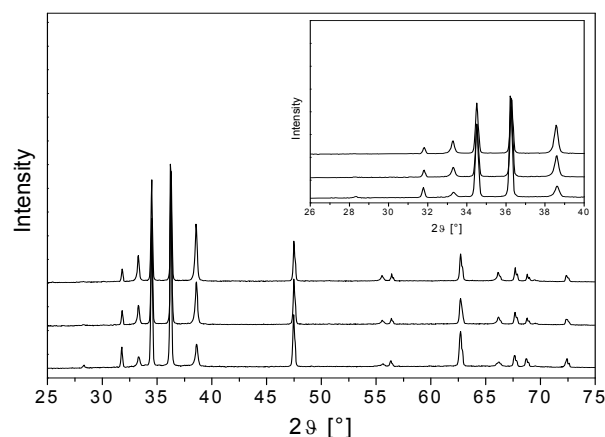


Fig. 7. Diffraction patterns of sample 0202 at 1000 °C

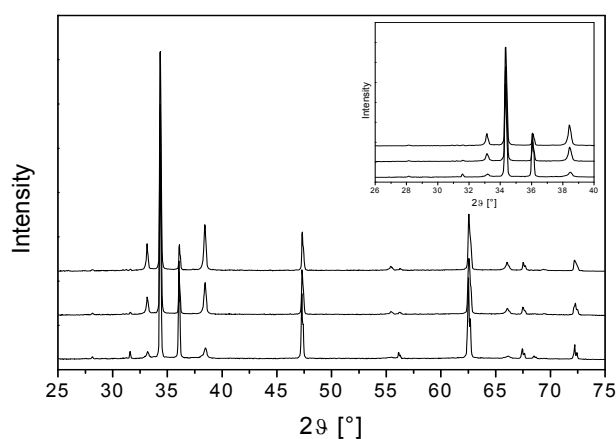


Fig. 8. Diffraction patterns of sample 0207 at 1000 °C

After the exposition the structure of α -Zr phase become considerably coarse. The structure of sample 0201 is homogeneously coarse-grained due to relatively fast heating without the deaeration step.

The α -Zr lines of samples 0202 and 0203 are created by single points with high intensity.

These points represent coherently diffracting large crystallites. The diffraction patterns are similar because there was relatively small difference in delivered energy. The α -Zr structure of the sample 0207 was very coarse-grained because the energy delivered during the heating was much higher than that in case of previous samples. The smooth continuous lines in all diffraction patterns belong to ZrO phase.

The amount of ZrO phase was growing with an energy delivered during the exposition, which directly influenced the course of indentation hardness and modulus of elasticity, Fig. 10. During the high-temperature heating at first the corrosion layer is growing up. After that this layer is disintegrated and the free oxygen diffused to inner volume of material where the ZrO phase is created, Fig. 6.

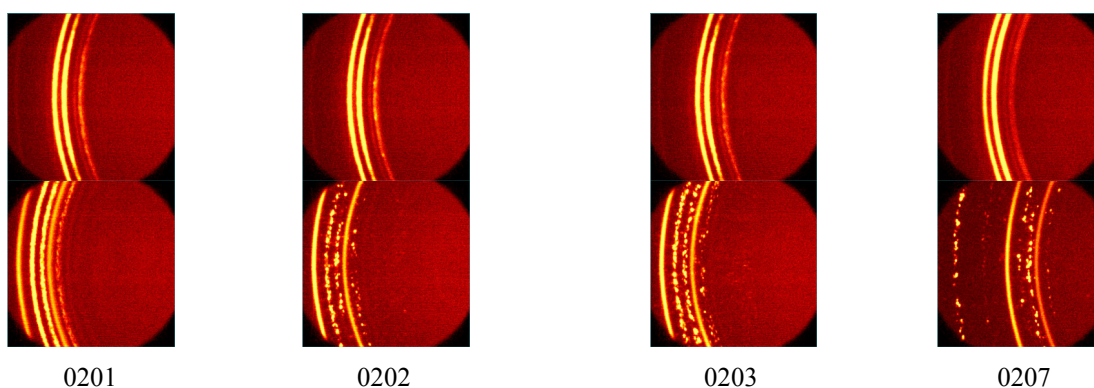


Fig. 9. Partial diffraction patterns measured by Bruker D8, upper pictures - initial state, bottom pictures – state after the exposition

Fig. 11 shows a dependence of indentation hardness on displacement into the surface. Apparently the hardness values of all samples in depth 2 μm are practically stable. That is why these values were taken as conclusive.

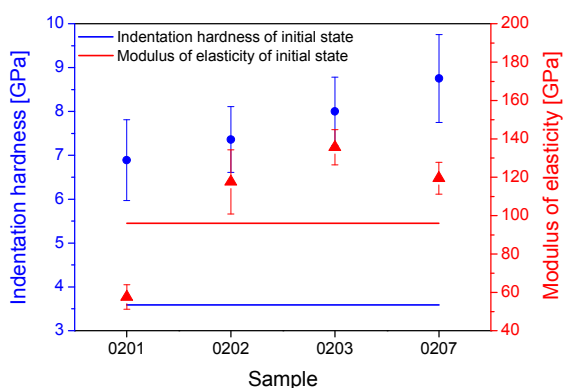


Fig. 10. Course of Indentation hardness and Modulus of elasticity

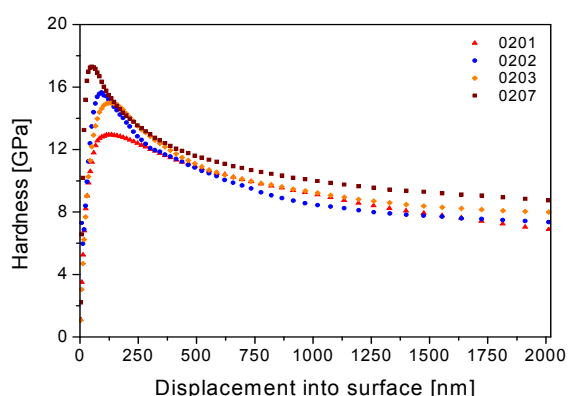


Fig. 11. Course of measured values of indentation hardness in dependence on displacement into surface

4. Conclusions

The results of XRD analysis and indentation hardness measurements presented that oxygen is probably the most important element influencing properties of Zr alloys. The XRD analysis demonstrated that corrosion layer formed during the heating, subsequently desintegrated and the free oxygen caused creation of ZrO phase. The amount of this phase grew with an exposition time at high temperature and caused the alloy hardness increasing. XRD analysis also indicated that vacuum value had only insignificant influence on properties of this type of alloy.

The work is supported by the MPO CR project 2A – ITP1/037.

REFERENCES

1. Koutský J., Kočík J.: *Radiation damage of structural materials*. Academia, Praha 1994.
2. Pétigny N., Barberis P., Lemaignan C., Valot Ch., Lallemand M.: *J. Nuclear Mater.* 280, 318 (2000).
3. Říha J., Bláhová O., Šutta P.: *Chem. Listy*, v tisku.
4. Baker H. (ed.): *ASM Handbook*, vol. 3, Alloy Phase Diagrams, ASM International, Materials Park, Ohio 1992.

J. Říha, O. Bláhová, and P. Šutta (*New Technologies – Research Centre, University of West Bohemia, Plzeň, Czech Republic*): **Mechanical Properties and Structure of Zr-Nb Alloy after High-Temperature Transformations**

The paper deals with study of phase transformations of Zr-Nb alloy and its influence on mechanical properties. For the experiment *in-situ* XRD analysis and indentation hardness measurements were used. The XRD measurements proceeded in evacuated high-temperature chamber with different heating process for each sample.

NANOINDENTATION AS A NEW TOOL FOR EVALUATION OF HEN'S EGGSHELL LOCAL MECHANICAL PROPERTIES

**LIBOR SEVERA^{a*}, JAROSLAV
BUCHAR^a, JIŘÍ NĚMEČEK^b,
and ŠÁRKA NEDOMOVÁ^a**

^a Mendel University of Agriculture and Forestry in Brno, Faculty of Agronomy, Zemědělská 1, 613 00 Brno, Czech Republic, ^b Czech Technical University in Prague, Faculty of Civil Engineering, Thákurova 7, 166 29 Praha 6, Czech Republic
severa@mendelu.cz

Keywords: eggshell, micro-mechanical properties, nanoindentation, elastic constants

1. Introduction

Elastic properties belong to the key engineering properties of an eggshell material. Their knowledge enables us to evaluate material stiffness that is further related also to the eggshell strength which is an important parameter of the eggs' quality¹⁻⁴. There are many techniques for the evaluation of main elastic properties, namely the Young's modulus E . Generally, they include static loading (mainly quasi-static compression)⁵⁻⁷ and different kinds of dynamic loading⁸⁻¹⁰. The evaluation of the elastic properties is mainly based on the assumption of the homogeneous and isotropic behavior of the eggshell. The eggshell is a bioceramic material constructed of columnar calcite crystals preferentially oriented with their c -axis perpendicular to the shell surface. The detail analysis revealed the microstructure varies through the thickness of the eggshell, so that the elastic properties must be expected to differ from the in-plane directions. However there is a little evidence to expect directional variations in properties in the plane of the eggshell. In order to examine these changes new techniques are needed. Nanoindentation seems to be a very promising procedure. The method is based on the direct measurement of the load-displacement relationship using a very small tip pressed into the material surface. The depth of penetration starts from the nanometer scale. Nanoindentation was originally developed and used mainly for studying of homogenous materials such as metals, coatings, glass and crystal materials. Successive evolution of the method led to testing of less conventional materials, some of which are of biological nature.

The objective of the present study was to investigate the potential utilization of nanoindentation as a tool for determination of eggshell's micro-mechanical properties

and to compare the experimental results with results obtained from conventional tests.

Finally it must be mentioned that, as it results from findings documented in literature, mechanical properties of hen's eggshell are strongly affected by many factors such as diet¹²⁻¹⁴, breeding conditions^{15,16}, hen breed^{17,18}, egg shape^{6,19,20} and other parameters under both static and dynamic loading. Thus single variable evaluation must be considered carefully and with respect to the previous facts.

2. Materials and Methods

2.1. Eggshells

Eggs (*Hisex Brown* strain) were collected from a commercial breeding farm in the Czech Republic. Hens were kept in cage technology. Eggs were collected when the hens were 75 weeks old. Double-yolked eggs, rough shelled eggs and abnormally shaped eggs were not included in the experiment.

2.2. Preparation of specimens

The eggshell chips from equatorial position on the egg were embedded into metacrylate tablet. The specimens were cold-prepared (the structure was not thermally affected). Commercially available two-component resin was used for metacrylate mixture preparation and the specimens were left to dry and cure for 8 hours. The tablets were polished in order to achieve flat surface with maximum roughness of 10-20 nm.

2.3. Experimental set-up and loading conditions

Nanohardness tester CSM was used to perform the experiments. Standard Berkovich tip was brought to the sample surface producing a series of imprints. Load versus depth of penetration was measured through the whole procedure of loading, holding, and unloading (see Fig. 2 for an example). Loading and holding parts of the diagram contain elastic, plastic and viscous deformations, whereas the unloading part is usually supposed to be elastic. Elastic constants were extracted from this unloading part using semi-analytical elastic solutions¹¹.

The eggshell chips (from equatorial position of the egg) were loaded in both radial (i.e. perpendicular to the surface) and tangential (i.e. parallel with the surface) directions. The set-up is shown in Fig. 1. Standardly used trapezoidal loading diagram with linear loading, unloading and intermediate holding period was performed.

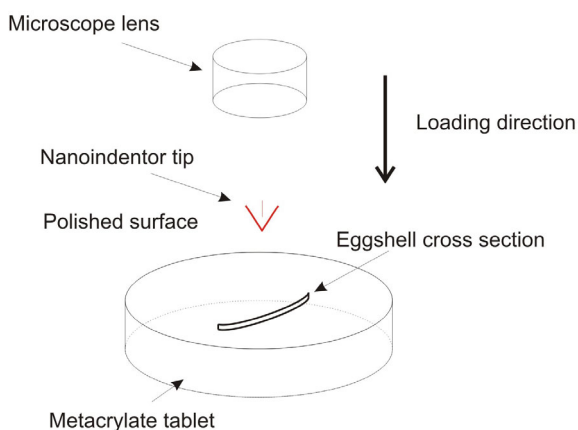


Fig. 1. Experimental set-up and loading in tangential direction

3. Results and discussion

Series of experiments containing around 25 measuring points on several cross sectional locations in two loading directions (radial and tangential) described above has been performed. For illustration, the overall view (200 \times magnification) on the eggshell cross section is shown in Fig. 3. The beads or little circles in the picture represent undissolved particles of metacrylate. The detailed view of an individual imprint of the indenter tip is depicted in Fig. 4.

An example of a typical loading diagram is shown in Fig. 2. Loading parameters with the main results are summarized in Tab. I.

Evaluation of the Young's modulus¹¹ includes the choice of Poisson's ratio ν . The value $\nu=0.345$ has been adopted from measurement described in Nedomová et al.⁶, where the similar eggshells were used (the research was conducted in parallel with this one and the same eggs were used). Other authors report similar values of ν , e.g. 0.307

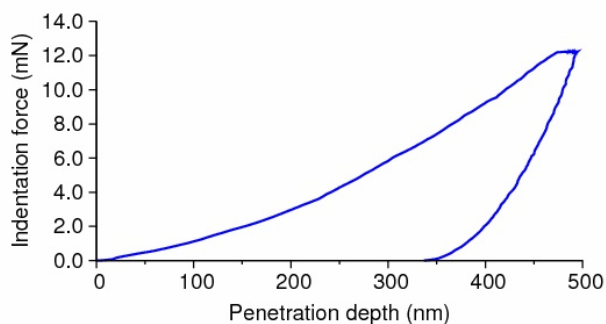


Fig. 2. Typical nanoindentation loading diagram (load vs. depth of penetration)

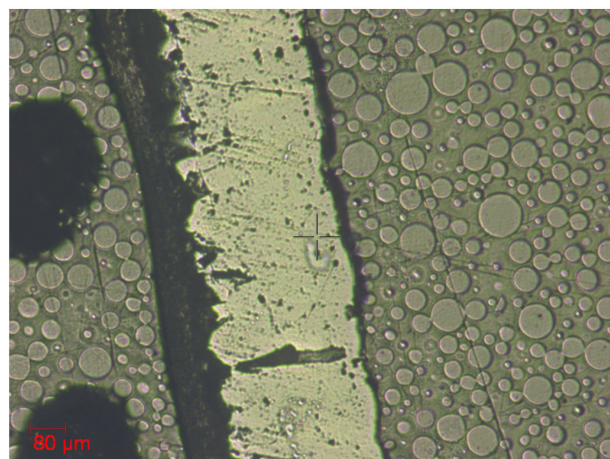


Fig. 3. Overall view on the eggshell cross section

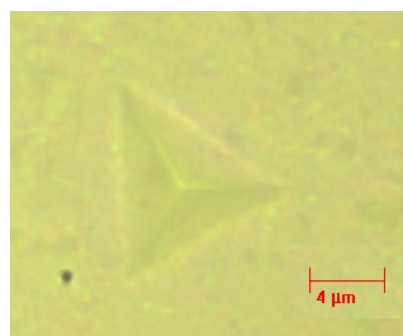


Fig. 4. Individual indenter imprint as seen in optical microscope (4000 \times magnification)

Table I
Experimental parameters and results

Peak load	10–12 mN
Loading rate	20 mN min ⁻¹
Unloading rate	20 mN min ⁻¹
Holding period	10.0 s
Young's modulus – radial loading	41 \pm 3.9 GPa
Young's modulus – tangential loading	43 \pm 4.1 GPa

(ref.²¹) or 0.300 (ref.⁸) but in these cases different eggs (hen strain, age etc.) were used.

The values of E obtained from radial and tangential directions did not vary significantly (41 \pm 3.9 GPa and 43 \pm 4.1 GPa, respectively). This scatter indicates isotropic nature of the eggshell structure. Due to small number of tests, this conclusion has to be confirmed by further and more detailed experiments, but it already shows on the general trend.

The E values did not significantly vary when testing different locations over the cross section which again shows on homogenous nature of the tested material. The possible edges, membrane, inhomogeneities and pores were avoided in the measurements. As can be seen in Fig. 4, the surface structure appears to be fairly homogenous, which supports the micromechanical measurements.

Young's moduli obtained from nanoindentation are in general agreement with values reported by Nedomová et al.⁶. Nedomová et al. found that elastic constants are independent on the egg shape as well as loading force orientation (egg loaded either on equator strip and/or egg-tip). The conclusions were supported also by numerical simulations.

4. Conclusions

The results obtained from nanoindentation in both radial and tangential directions of the eggshell equator revealed homogeneous nature of the material. Based on the limited number of experiments, it is assumed that local variation in the stiffness is not direction dependent and the tested material appears to be more or less isotropic.

It follows from macroscopic measurements that mechanical properties show certain degree of variability when measured at different locations on the same egg¹. Therefore, the use of nanoindentation for creating of a more detailed „map“ of eggshell's micromechanical properties from various locations seems to be a promising and probably one of very few applicable approaches. The research in this area is planned as a future goal.

Presented results approved that nanoindentation, as a novel testing method used for determining of eggshell micromechanical properties, offers a precise tool for describing material characteristics on eggshell micro-scale and thus offers precise and valuable data for mapping of material parameters, modeling, numerical simulations and procedures used for upgrading of the current state of knowledge at this particular field.

The research has been supported by the Grant Agency of the Czech Academy of Sciences under Contract No. IAA201990701 and Ministry of Education of the Czech Republic (Research Plan MSM 6840770003).

REFERENCES

1. Lin J., Puri V. M., Anantheswaran R. C.: *Transaction of the ASAE* 38, 1769 (1995).
2. Carnarius K. M., Conrad K. M., Mast M. G., Mac Neill J. H.: *Poultry Sci.* 75, 656 (1996).
3. Nirasawa K., Takahashi H., Takeda H., Furukawa T., Takeda T., Nagamine Y.: *J. Anim. Breed. Genet.* 115, 375 (1998).
4. Picman J., Pribil S.: *J. Ornithology* 138, 531 (2002).
5. De Ketelaere B., Govaerts T., Coucke P., Dewil E., Visscher J., Decuypere E., De Baerdemaeker J.: *Br. Poult. Sci.* 43, 238 (2002).
6. Nedomová Š., Severa L., Buchar J.: *Int. Agrophysics* 23, 249 (2009).
7. Buchar J., Simeonovová J.: 19th CAD – FEM USERS MEETING 2001, *International Congress on FEM Technology, 17-19.October 2001, Potsdam, Berlin.*
8. Coucke P.: *PhD Thesis*, KU Leuven 1998.
9. Severa L.: *Acta of Mendel University of agriculture and forestry Brno = Acta Universitatis agriculturae et silviculturae Mendelianae Brunensis* 55, 137 (2007).
10. Nedomová Š., Trnka J., Dvořáková P., Buchar J., Severa L.: *J. Food Eng.* 94, 350 (2009).
11. Oliver W. C., Pharr G. M.: *J. Mater. Res.* 7, 1564 (1992).
12. De Andrade A. N., Rogler J. C., Featherston W. R., Alliston C. W.: *Poult. Sci.* 56, 1178 (1977).
13. Grizzle J., Iheanacho M., Saxton A., Broaden J.: *Br. Poult. Sci.* 33, 781 (1992).
14. Lichovníková M., Zeman L., Jandásek J.: *Czech J. Anim. Sci.* 53, 7 (2008).
15. Emery D. A., Vohra P., Ernst P. A., Morrison S. R.: *Poult. Sci.* 63, 2027 (1984).
16. Lichovníková M., Zeman L.: *Czech J. Anim. Sci.* 53, 162 (2008).
17. Máchal L., Jeřábek S., Zatloukal M., Straková E.: *Czech J. Anim. Sci.* 49, 51 (2004).
18. Máchal L., Simeonovová, J. – *Archiv fur Tierzucht* 45, 287 (2002).
19. Anderson K. E., Tharrington J. B., Curtis P. A., Jones F.T.: *Int. J. Poult. Sci.* 3, 17 (2004).
20. Havlíček M., Nedomová Š., Simeonovová, J., Severa L., Křivánek I.: *Acta Universitatis agriculturae et silviculturae Mendelianae Brunensis* 56, 69 (2008).
21. Lin H., Mertens K., Kemps B., Govaerts T., De Ketelaere B., De Baerdemaeker J., Decuypere E., Buyse J.: *Br. Poult. Sci.* 45, 476 (2004).

L. Severa^a, J. Buchar^a, J. Němeček^b, and Š. Nedomová^a (^aMUAF in Brno, ^bCTU in Prague): **Different Methods of Evaluation of Hen Eggshell Mechanical Properties**

The paper studies suitability and applicability of nanoindentation as a method used for assessment of hen's eggshell local micromechanical properties. The eggshells were tested in the area surrounding equator line. The values of Young's modulus E obtained from radial and tangential directions did not vary significantly (41 ± 3.9 GPa and 43 ± 4.1 GPa, respectively). This fact shows on isotropic nature of eggshell structure. It was found that values of E does not significantly change across the cross sectional area. The values obtained within this research correspond to values reported in literature and obtained on macroscopic samples. Nanoindentation was found to be a precise and powerful tool, suitable for determining local variations of mechanical properties of eggshells.

EFFECT OF TEMPERATURE AND GASEOUS MEDIUM ON THE STRUCTURE AND MICROHARDNESS OF THE COBALT BASE CLAD LAYERS

HANNA SMOLENSKA*

*Gdansk University of Technology, Faculty of Mechanical Engineering, Department of Materials Science and Engineering, 11/12 Narutowicza str., 80-233 Gdańsk, Poland
hsmolens@pg.gda.pl*

Keywords: cobalt alloy, oxidation, hardness

1. Introduction

The engines, gas turbine or industrial applications like for example: moulds for glass and ceramics, automotive valves, chemical and petrol-chemical valves need special material. For such a severe service conditions materials must have high strength and adequate resistance to gaseous corrosion at elevated temperatures. There are a wide range of compositions based on nickel, cobalt and nickel-iron. Their various applications are based largely on their suitability at higher temperatures to a particular environment. During recent decades, the high-temperature oxidation of structural materials, such as Fe-, Co-, and Ni-base alloys, for which high-temperature oxidation resistance is an important parameter, has been investigated intensively. In general, these alloys, developed good resistance to hot corrosion gases by possessing proper amounts of Al, Cr, and Si and are called as alumina, chromia, and silica formers. For chromia formers, maximum protection against oxidation is obtained only if a continuous and coherent Cr_2O_3 scale layer is formed and maintained. That alloys must have a sufficient chromium content to initially form a chromium oxide and supply of chromium by diffusion within the underlying alloy in order to continuous growth of the protective scale¹⁻³. In spite of the long history of the investigation of oxidation and oxide scales, there are still many aspects of this phenomenon that are not well understood. Our incomplete understanding of scale formation and evolution is due to both the extraordinary complexity of the process and the limited availability of tools that allow a complete characterization of the scales themselves⁴⁻⁶. The growing of the protective oxide scale must cause different processes which involve selective oxidation of alloy elements and lead to changing of the alloy composition in the subsurface region and even phase transformation may occur. Typically it is scale formation and subsurface degradation. As the time passed the scale may change its chemical composition. The degradation of the alloy may be a result of phase formation or dissolution and formation of voids⁷⁻⁹. Not only corrosion resistance is desirable but also the mechanical properties like: high temperature

strength, fatigue strength, hardness, creep and wear resistance.

2. Experimental

In this work the cobalt base clad layers were examined. They were produced on the face of the exhaust valve head of the marine diesel engine in order to prolong service time of this part. The substrate material was A-R-H10S2M (X40CrSiMo10-2) steel. The equipment used for the plasma transferred arc (PTA) cladding was a CASTOLIN EUTRONIC GAP 200. The layer consisted of three sublayers with three tracks for each one. The subsequent tracks were overlapped by 30–40 %. The powder was delivered straight to the melt pool. The chemical composition of the powder was as follow: C – 1,32 %, Si – 1,25 %, Cr – 29 %, W – 5,3 %, Ni – 2,1 %, Mo – < 0,1 %, Fe – 1,9 %, and Co as balance. After cladding the layer underwent turning in order to obtain proper geometry. The prepared base materials – exhaust valve – covered with clad layers was cut into pieces and then heat-treated under different conditions. The conditions were as follow: isothermal oxidation at 750 °C for 200 hours, isothermal oxidation at 850 °C for 200 hours, cyclic oxidation at 1100 °C for 100 hours (100 cycles) and cyclic corrosion in exhaust gases at 750 °C for 200 hours. The response of the coating to the elevated temperature was illustrated by the microstructural changes and microhardness profiles of the cross-section of the specimens. After metallographic preparation, the cross-sections were examined. The analytical techniques used to characterize the samples included optical microscopy, scanning electron microscopy (SEM), energy dispersive spectroscopy (EDS) and X-ray powder diffraction (XRD). SEM was conducted at accelerating voltages ranging from 15–30 kV in backscattered and secondary electron imaging modes. Mechanical properties were represented by hardness measurement on the cross-section.

3. Results and discussion

3.1. Microstructure investigation

The cross-section of the hardened layer on the valve presented typical welding solidification structures for as-deposited state. This microstructure can be described as a Co rich matrix with a network of carbides and eutectics in the interdendritic regions¹⁰⁻¹² (Fig. 1). Cross-section EDAX analysis of the clad layers revealed that the matrix was enriched in chromium and tungsten. Eutectics were

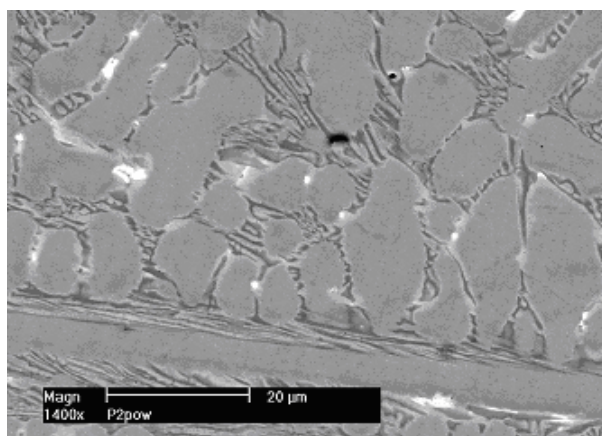


Fig. 1. SEM - Cross-section of the cobalt base layer as clad

enriched in chromium, tungsten and silicon¹³. After oxidation the changes in microstructure were dependent on oxidation temperature and distance from the surface.

After 750 °C oxidation treatment the oxide scale was very thin and almost difficult to observe on the cross section of the sample. The higher temperatures, 850 and 1100 °C, caused forming thicker oxide scales and also internal oxidation region was observed after 1100 °C processes. In the bulk of the layer not visible changes were noticed. Cross-section EDAX analysis of oxidized laser clad revealed that the uppermost part of the scale has relatively high concentration of Cr and O while the amount of Co remained unchanged¹³. It suggested the formation of Cr-rich outer oxide scale and relatively less Cr amount just under the scale. The other elements did not indicate any changes. After heating at 850 °C, the scale was dense, an approximately 6 μm thick (Fig. 2).

For this case under the dense scale layer the negligible traces of internal oxidation were noticed only on the boundaries of some dendrites. The degradation of clad

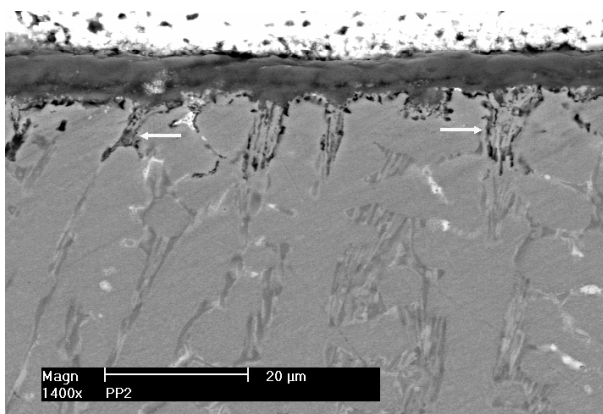


Fig. 2. SEM - Cross-section of the clad layer after oxidation at 850 °C. The arrows indicate the internal oxidation traces

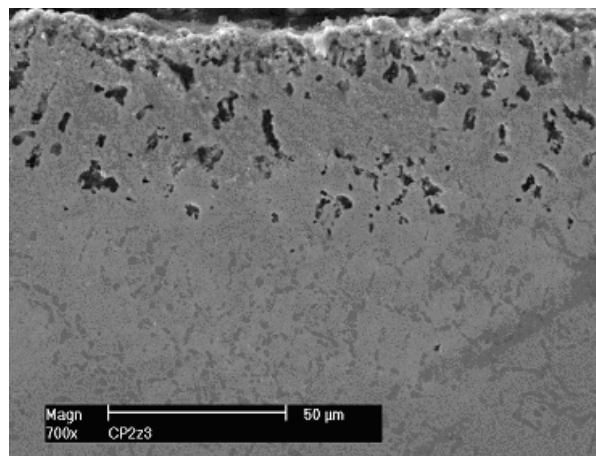


Fig. 3. SEM - Cross-section of the clad layer after oxidation at 1100 °C

material reached no more than 34 μm. The XRD analysis revealed generally Cr₂O₃ (ref.¹³) presence in the scales. The scale and the degradation of the clad after oxidation at 1100 °C (Fig. 3) were more critical. The scale was thicker, uniform and partially showed tendency to spalling. This led to disappearance of the carbides and degradation of the interdendritic regions in the cobalt alloy under the scale. The degradation of clad material reached about 60 μm.

After corrosion in exhaust gases the scale on the surface of the clad was so thin that it was difficult to notice on the samples' cross-section because during the metallographic preparation it was difficult to get sharp edge. However the observation of the top of the valve face confirmed the presence of the oxide layers. In the case of corrosion in exhaust gases scale composition appeared different. The scale was much thinner and consisted of chromium and iron oxides and possible small amount of sulfides. The chromium decrease under the scale was less noticeable.

3.2. Microhardness measurement

For hardness measurement the GOST 7865–86 manual microhardness tester was used. The test was carried out on the finely polished transversally sectioned surface perpendicular to the surface of the layer, at the load of 200 g for a loading time of 20 s. This load produced clear indentation, easy for optical measurement and small enough for proceeding hardness measurements within the space 0,2 and even 0,05 mm. The first measured point was placed at the distance 0,05 mm from the clad surface. For the next points the distances between them were 0,2 mm. On the clad-steel interface the points were situated at 0,05 mm distance on both sides of the fusion line. Because of hardness variation across the layer the 3 series of measurement were made. Fig. 4 presents the hardness profile of the clad and steel base just after cladding.

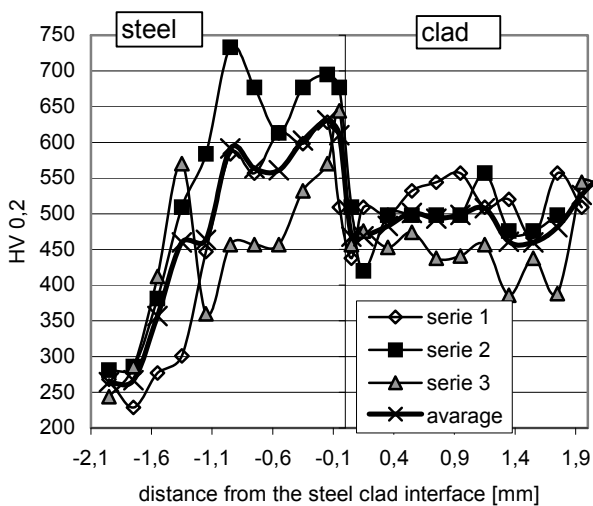


Fig. 4. Microhardness measurement for as-clad layer and steel base

The non-uniform hardness across the coating was a result of multilayer producing process and structure of this layer. The heat affected zone (HAZ) was observed in the steel under the clad layer. From the morphological point of view, the measured differences in hardness were affected by the dendrite structure and can also be attributed to the morphology of the carbides^{11,12}. This phenomenon is related to the multiple heating and cooling during the multi layer cladding process. The heat treatment in different temperatures and atmospheres led to the changes in the hardness especially in the upper part of the clad.

Even for the low temperature (750 °C) heat treatment, when changes in microstructure were negligible the hardness decrease was observed (Fig. 5, 6).

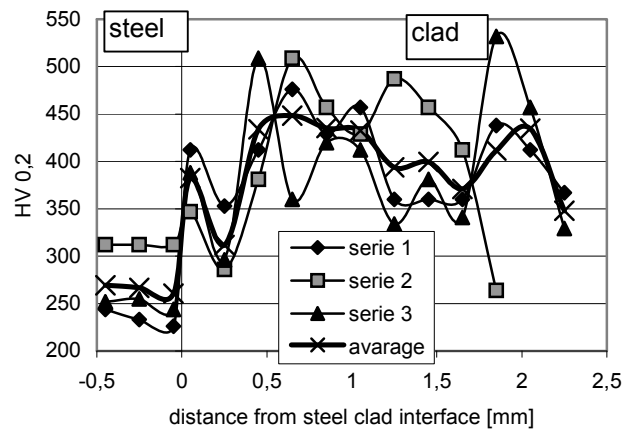


Fig. 6. Microhardness measurement after corrosion in exhaust gases at 750 °C

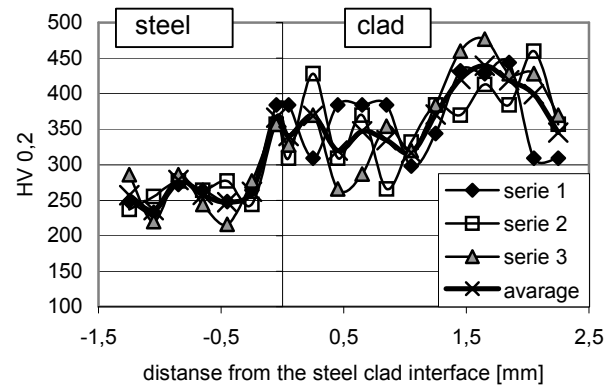


Fig. 7. Microhardness measurement after oxidation at 850 °C

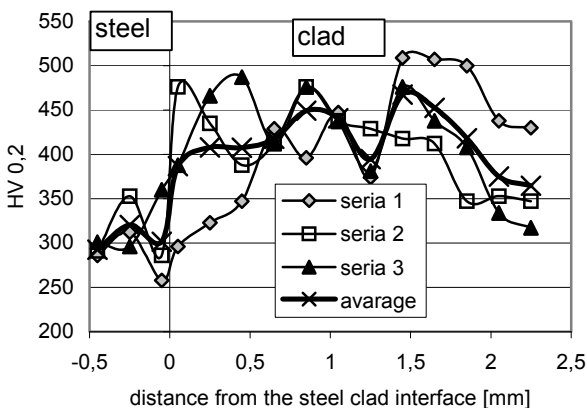


Fig. 5. Microhardness measurement after oxidation at 750 °C

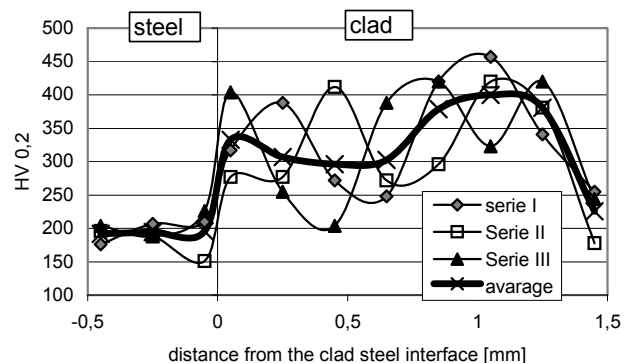


Fig. 8. Microhardness measurement after oxidation at 1100 °C

After treatment at higher temperatures the hardness decreases were obvious and corresponded with the microstructure changes (Fig. 7, 8).

For all temperatures the hardness decreased in the HAZ. It was a result of the temperature influence. The oxidation treatment acted as annealing process and removed microstructural changes typical for HAZ. As a result the HAZ zone disappeared.

4. Conclusion

For the conditions tested the results led to some important conclusions:

- The oxidation reaction in investigated alloy was initiated by the formation of the outer scale of chromia which was nucleated and subsequently grew in thickness by diffusion and caused depletion the underlying alloy of chromium. The high chromium content carbides situated on the dendrite boundaries were the main source of the chromium. The decomposition of the carbides led to degradation of the dendrite boundaries and caused the voids formation. The increase of the oxidation temperature strongly influences the thickness of the material which underwent the degradation process.
- In the outer surface sublayer with thickness of about 0,3 mm, a significant decrease of hardness was found. This observation correlated with the microstructural changes that are the disappearance of carbides in the interdendritic region and their replacement by Cr-oxide.
- The correlation between hardness and microstructure of clad layers was proved for as –clad and after oxidation state.
- The microhardness measurement is more sensitive on material changes due to the heat treatment than microstructural analyzes.

REFERENCES

1. Gleeson B., Harper M. A.: *Oxid. Metals* 49 (3/4), 1998.
2. Gleeson B., Harpe M. A.: *Oxid. Metals* 49 (3/4), 1998.
3. Yuan F., Sun X., Guan H., Hu Z.: *J. Chinese Society of Corrosion and Protection* 22 (2), 2002.
4. Uran S., Veal B., Grimsditch M., Pearson J., Berger A.: *Oxid. Metals* 54 (1/2), 2000.
5. Yang F. M., Sun X. F., Guan H. R., Hu Z. Q.: *Metall. Mater. Trans. A* 34, 979 (2003).
6. Berthod P., Michon S., Aranda L., Mathieu S., Gachon J.C.: *Comput. Coupling Phase Diagrams Thermochem.* 27, 353 (2003).
7. David J. Young, Brian Gleeson: *Corros. Sci.* 44, 345 (2002).
8. Douglass D. L., Armijo J. S.: *Oxid. Metals* 3 (2), 1971.
9. Jones D. E., Stringer J.: *Oxid. Metals* 9 (5), 1975.
10. Liu P.S., Liang K.M.: *Oxid. Metals* 53, 351 (2000).
11. Hou P. Y., Stringer J.: *Oxid. Metals* 33 (5/6), 1990.
12. Li B., Gleeson B.: *Oxid. Metals* 65, 101 (2006).
13. Smolenska H.: *Adv. Mater. Sci.* 7, 254 (2007).

H. Smolenska (*Gdansk University of Technology, Poland*): **Effect of Temperature and Gaseous Medium on the Structure and Microhardness of the Cobalt Base Clad Layers**

The influence of oxidation temperature on the hardness and microstructure of Co-base alloy coatings were investigated. Coatings were manufactured by PTA cladding on a valve steel X40CrSiMo10-2 substrate. The cobalt alloy was exposed to high temperatures in air from 750 °C to 1100 °C and in exhaust gases at 750 °C. As a result of oxidation treatment the changes in microhardness for cobalt layers were observed. In the outer surface sublayer with thickness of about 0,3 mm a significant decrease of hardness was found. The higher temperature was applied, the bigger decrease of hardness was observed. The hardness measurement presents more sensitive reaction on material changes during the heat treatment than microstructural analyzes.

COULD HUMIDITY AFFECT THE MECHANICAL PROPERTIES OF CARBON BASED COATINGS?

JAROSLAV SOBOTA^{a*}, JAN GROSSMAN^a, JIŘÍ VYSKOČIL^b, RUDOLF NOVÁK^c, TOMÁŠ FORT^a, TOMÁŠ VÍTU^d, and LIBOR DUPÁK^a

^a Institute of Scientific Instruments, Academy of Sciences of the Czech Republic, Královopolská 147/62, 612 64 Brno,

^b HVM Plasma Ltd. Na Hutmance 2, 158 00 Praha 5,

^c Faculty of Mechanical Engineering, Czech Technical University, Technická 4, 166 07, Praha 6, ^d Faculty of Transportation Sciences, Czech Technical University, Na Florenci 25, 110 00, Praha 1, Czech Republic

sobota@isibrno.cz

Keywords: coatings, carbon, mechanical properties, humidity, fracture toughness

1. Introduction

We evaluated the effect of humidity on tribological behaviour¹ and impact resistance at elevated temperatures of carbon-based hard composite coatings deposited by PACVD with an interface metallic layer prepared by unbalanced planar magnetron sputtering. These layered systems are intended to be used as a protective coatings in car engine components exposed to a dynamic load. To evaluate the impact resistance of thin hard composite coatings in dynamic loading wear applications an impact test was used. Impact testing of coatings was proposed by Knotek et al. in the 1990's (ref.²). During this testing, the specimen was cyclically loaded by a tungsten carbide ball that impacted against the coating-substrate surface. Both impact tests and wear test with linear reciprocating movement were made in dry and humid air.

2. Experimental Details

Carbon-based composite coatings were prepared in industrial equipment by a combined PVD/PACVD (physical vapour activated deposition) process. An interface metallic layer prepared by unbalanced planar magnetron sputtering and DLC (diamond like carbon) coating was deposited by PACVD with pulsed bias from hydrocarbon gases. HSS (high speed steel) was used as a substrate material and polished to Ra of about 0.05 μm . Total thickness of the coating determined by the calotest method was about 2.5 μm .

The impact tester developed at the Institute of Scientific Instruments ASCR, Brno was modified for measurements in controlled environment, to evaluate the possible influence of humidity on the impact resistance of coating-substrate system, Fig. 1.



Fig. 1. Impact tester developed at the Institute of Scientific Instruments ASCR, Brno for measurement in controlled environment

A reciprocal tribometer with controlled humidity was used to study friction/wear properties of coatings, Fig. 2. Normal and tangential loads measured by tensiometers are recorded every 10–50 ms. Typical parameters include a normal load of 5–30 N.

A high temperature tribometer (CSM Instruments) was used to measure friction and wear characteristics of



Fig. 2. Reciprocal tribometer developed at HVM Plasma Ltd



Fig. 3. High temperature CSM tribometer

coatings at an elevated temperature, Fig. 3. The principle of measurement is the pin-on-disc method with rotating disc and this measurement is considered as a “standard”.

The pin is mounted on a stiff lever designed as a frictionless force transducer. As the sample is rotating, the effect resulting friction forces between the pin and the sample is measured through very small deflection of the lever. This device allows to carry out precisely calibrated friction and wear measurement at temperatures ranging from the room temperature (RT) up to 800 °C with these main specifications: rotational speed 1 to 500 rpm, forces up to 10 N and maximum disc dimensions: Ø 60 mm × 15 mm.

3. Results

3.1. Impact Tests

In Fig. 4 we can see the dependence of the crater volume created during impact testing of the coated sample on the number of impacts^{2,3}.

The tests were carried out at the relative humidity (RH) levels of 2.5 % and 95 % at an impact force of 600 N.

Mean values are indicated with marked error bars. As a ratio of the number of impacts and volume of the crater, the dynamic impact resistance was calculated. At the relative humidity of 2.5 %, the dynamic impact resistance was $2.17 \cdot 10^4$, but at RH 95 % it reached $9.09 \cdot 10^4$. That means that the value of dynamic impact resistance increased more than four times.

Upon comparing measured of crater volumes, we can see, that the relative humidity substantially influences dynamic resistance of the coating-substrate system, in particular in the region of mechanical erosion of the coating

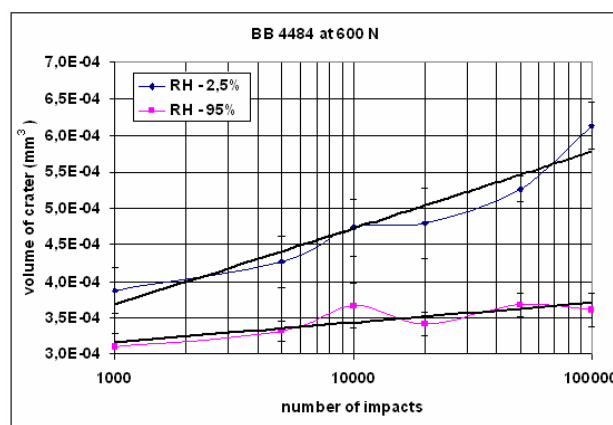


Fig. 4. The dependences of the crater volume created during impact testing of the coated sample on the number of impacts obtained at an impact force of 600 N measured at the relative humidity levels of 2.5 % and 95 %

3.2. Reciprocal Tribometer

In Fig. 5, the enormous influence of humidity on the coefficient of friction and wear rate of the coating can be observed. By increasing the RH from 0 % to 80 %, the wear rate of the coated part increases by more than four orders of magnitude. The effect of humidity on the coefficient of friction cannot be neglected either.

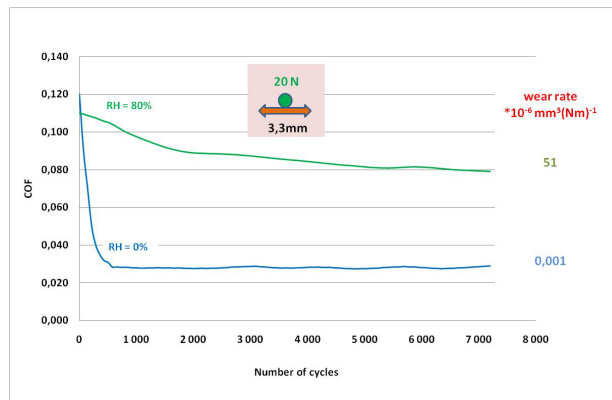


Fig. 5. Coefficient of friction (COF) and wear rate measured on the reciprocal tribometer at the relative humidity levels of 0 % and 80 %

3.3. High Temperature CSM Tribometer

The typical friction curves of a hard coating sliding against a 100Cr6 ball at room temperature, 120 °C and 200 °C are given in Fig. 6. All measurements were performed at the load of 15 N and a linear speed of 4 cm s^{-1} , with the relative air humidity of $25 \pm 5 \%$. The first part of the curve, the run-in stage, was represented by a strong

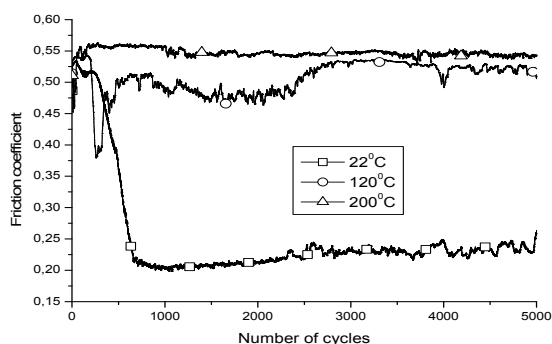


Fig. 6. Friction curves of the hard coating sliding against a 100Cr6 ball measured on a high temperature CSM tribometer at the room temperature, 120 °C, and 200 °C

increase in the coefficient of friction during the first cycles to a high value of 0.53.

In the next 700 cycles, the coefficient of friction dropped to a lower level. The following part, in which the coefficient of friction remained constant until destruction of the coating, was determined as the steady-state wear. The coefficient of friction during the steady-state wear stage depended essentially on temperature. At RT the reactions of the ball surface with oxygen and water played a significant role resulting in a low value of coefficient of friction. Drying of the coating and ball surfaces at a temperature above 100 °C resulted in an increase of the coefficient of friction. By additionally elevating the temperature, the formation of oxides species was expected and it took effect in a substantial increase of the coefficient of friction.

4. Conclusion

Humidity can significantly influence not only the tribological behaviour of carbon-based coatings¹, but unexpectedly, as we discovered, also their impact resistance.

By increasing the relative humidity, the dynamic impact resistance increases more than four times. Simultaneously, the wear rate of the coated part increases by more than four orders of magnitude. The coefficient of friction during the steady-state wear stage depends essentially on temperature. At RT, the coefficient of friction has a low value. Drying of the coating and ball surfaces at temperatures above 100 °C results in an increase in the coefficient of friction.

In optimising the coated car engine components exposed to dynamic loads, we must take into account not only the temperature, roughness of surfaces, and contact pressure but also the influence of the relative humidity at which the component runs.

This work has been supported by a grant from the Czech Ministry of Industry and Trade MPO 2A-ITP1/031.

REFERENCES

1. Svahn F., Kassman-Rudolphi A., Hogmark S.: *Wear* 261, 1273 (2006).
2. Knotek O., Bosserhoff B., Schrey A., Leyendecker T., Lemmer O., Esser S.: *Surf. Coat. Technol.* 54/55, 102 (1992).
3. Engel P. A., Yang Q.: *Wear* 181-183, 730 (1995).

J. Sobota^{a*}, J. Grossman^a, J. Vyskočil^b, R. Novák^c, T. Fořt^a, T. Vítu^d, and L. Dupák^a (^a *Institute of Scientific Instruments, Academy of Sciences of the Czech Republic, Brno*, ^b *HVM Plasma Ltd., Praha 5*, ^c *Faculty of Mechanical Engineering, Czech Technical University, Praha 6*, ^d *Faculty of Transportation Sciences, Czech Technical University, Praha 1, Czech Republic*): **Could Humidity Affect the Mechanical Properties of Carbon Based Coatings?**

We evaluated the influence of humidity on tribological behaviour, impact resistance and tribological behaviour at elevated temperatures of carbon-based hard composite coatings deposited by PACVD with an interface metallic layer prepared by unbalanced magnetron sputtering.

Impact tests were carried out at a relative humidity of 2.5 % and 95 % at an impact force of 600 N. Comparing measured values of crater volumes we can see, that the relative humidity substantially influences dynamic resistance of the coating – substrate system, in particular in the region of mechanical erosion of the coating.

It is well known for years, that humidity can significantly influence the tribological behaviour of carbon-based coatings. However, unexpectedly, humidity also influences the impact resistance of this type of films. By increasing the relative humidity, the value of dynamic impact resistance significantly increases. Simultaneously the wear rate of the coated part increases by many orders of magnitude. By optimising components coated by carbon-based coatings exposed to dynamical load, we must take into account not only temperature and, roughness of surfaces, but also the influence of the relative humidity at which the coating – substrate system runs.